Journal of Physics: Photonics

TOPICAL REVIEW

In vivo photoacoustic and ultrafast ultrasound Doppler assessment of vascularity for potential thyroid cancer diagnosis: a comprehensive review

Ninjbadgar Tsedendamba[1], **Jean-Claude Vial**[2], **Robert A Taylor**[3], **Jeesu Kim**[1,5,*] **and Wonseok Choi**[4,5,*]

[1] Department of Cogno-Mechatronics Engineering, College of Nanoscience and Nanotechnology, Pusan National University, Busan 46241, Republic of Korea
[2] Laboratoire Interdisciplinaire de Physique, Centre National de la Recherche Scientifique, Université Grenoble Alpes, 38000 Grenoble, France
[3] Department of Physics, University of Oxford, Oxford OX1 3PU, United Kingdom
[4] Department of Biomedical Engineering and Medical Sciences, College of Medicine, The Catholic University of Korea, Seoul 06591, Republic of Korea
[5] These authors are the co-corresponding authors and contributed equally.
[*] Authors to whom any correspondence should be addressed.

E-mail: jeesukim@pusan.ac.kr and wonseok.choi@catholic.ac.kr

Keywords: thyroid cancer, vascularity analysis, photoacoustic imaging, ultrafast Doppler imaging, clinical study

OPEN ACCESS

RECEIVED
28 October 2024

REVISED
12 February 2025

ACCEPTED FOR PUBLICATION
23 March 2025

PUBLISHED
1 April 2025

Abstract

Thyroid cancer remains prevalent worldwide, with its incidence steadily increasing in recent decades. Although ultrasonography is currently the primary screening method in clinical practice, its relatively low specificity has contributed to increased overdiagnosis. Furthermore, conventional ultrasonography is associated with challenges such as high inter- and intra-observer variability and limited functional imaging capabilities, which together reduce its diagnostic accuracy. To address these limitations, researchers have explored complementary image-based techniques to assess the vascularity surrounding cancerous nodules. This comprehensive review provides an overview of recent clinical trials investigating advanced ultrasound (US)-based imaging techniques for diagnosing thyroid cancer in humans. Specifically, we explore the use of photoacoustic imaging and ultrafast US Doppler techniques, highlighting their potential to enhance triaging accuracy by enabling the analysis of both structural and functional characteristics of thyroid nodules *in vivo*. Integrating these innovative approaches into existing ultrasonography protocols could significantly enhance the precision of thyroid cancer diagnosis.

1. Introduction

Thyroid cancer is one of the most frequently diagnosed cancers globally [1–5]. According to recent statistics from the American Cancer Society, approximately 44 020 new cases are expected to be diagnosed in the United States by 2024 [6]. The incidence of thyroid cancer has consistently increased over the past several decades [7–9]. In 2019, the age-standardized incidence rates in the United States were 20.5 and 7.9 per 100 000 person-years for women and men, respectively [6]. Despite this rising incidence, the mortality rate associated with thyroid cancer remains relatively low compared to other common cancers such as breast, prostate, lung, and colorectal cancers. This low mortality rate is primarily attributed to the overdiagnosis of small nodules. While detecting and treating small nodules that typically do not require urgent intervention reduce mortality, the overall diagnostic costs increase due to low specificity resulting from overdiagnosis [10–12]. 3%–8% of the United States population has detectable thyroid nodules, only 5%–15% of these nodules are malignant [13]. Diagnostic imaging techniques such as ultrasound imaging (USI), x-ray computed tomography (CT), and magnetic resonance imaging have enabled the detection of small benign nodules. However, these modalities often fail to definitively determine malignancy, potentially leading to unnecessary biopsies and surgeries, increased healthcare costs, and a negative impact on patients' quality of life [14].

Currently, the standard approach for assessing the risk of thyroid nodules involves evaluating their structural characteristics using ultrasound (US) images. The typical US-based risk stratification methods include the American Thyroid Association (ATA) Guideline [15], British Thyroid Association (BTA) Guideline [16], and Thyroid Imaging Reporting and Data System [17]. When a nodule exhibits malignant features such as size, taller-than-wide shapes, presence of calcifications, irregular margins, hypoechogenicity, and specific compositions (cystic, solid, or mixed) [18, 19], a fine-needle aspiration biopsy is typically performed to confirm a cancer diagnosis [20]. However, US-based risk stratification is often limited by its low specificity, leading to the misdiagnosis of benign cases and unnecessary biopsies or surgeries [21–23]. This limitation arises mainly because the US-based method relies solely on the morphological features of thyroid nodules.

To enhance diagnostic accuracy and reduce overdiagnosis, recent research has focused on addressing the lack of pathological information in conventional USI [24]. One branch of the study aims to obtain additional blood flow information through Doppler imaging and to analyze the amount of intranodular vascularity [25–27]. Studies incorporating vascularization parameters alongside traditional US-based features have demonstrated improvements in diagnostic accuracy. However, the increase in classification accuracy has been marginal, and some studies suggested that hypervascularization or specific blood flow patterns may not reliably indicate malignancy in thyroid nodules [28–31]. This ongoing debate is reflected in current guidelines, where intranodular hypervascularization is considered a malignancy risk factor in the BTA Guideline but not in the ATA Guideline [32].

To address these challenges, photoacoustic imaging (PAI) has been studied for thyroid assessment by visualizing molecular information on nodules and complementing conventional US-based risk stratification [33–35]. Considering their imaging principles, PAI and USI can be implemented in a single imaging platform, providing co-registered information of molecular optical absorption and morphological structure from simultaneously obtained PA and US images, respectively [36–39]. Advanced USI techniques using ultrafast plane-wave US, have employed to gain additional insights into thyroid nodules. In particular, ultrafast Doppler (UFD) imaging offers a more precise depiction of blood flow within thyroid nodules compared to conventional color or power Doppler techniques, allowing for the assessment of microvascular flows *in vivo* [40].

In this review, we provide an overview of the principles and characteristics of PAI and UFD, summarize recent advances in these technologies for analyzing thyroid nodules, and evaluate their potential for improving the triaging process. We also review recent clinical trials for diagnosing thyroid cancer in human subjects, highlighting their potential of these techniques to enhance triaging accuracy in clinical workflows. By integrating structural and functional information into existing US-based risk stratification methods, the accuracy of thyroid nodule assessment can be significantly improved.

2. Principles of imaging techniques

2.1. Principles of PAI

The main principle for PAI signal generation is the photoacoustic effect, which refers to the generation of acoustic pressure waves (i.e. PA waves) through the sudden thermal expansion and contraction of optical absorbers after pulsed illumination. The amplitude and frequency of the generated PA pressure waves depend on the illumination parameters and the optical absorption coefficient of the target. Most PA imaging systems use laser pulses with durations significantly shorter than the thermal and stress relaxation times, ensuring that the optical excitation phase satisfies the requirements of thermal and stress confinement. In this case, the initial PA pressure amplitude $p_0(\vec{r},\ \lambda)$ is proportional to the optical fluence $F(\vec{r},\ \lambda)$ (mJ cm^{-2}), optical absorption coefficient $\mu_a(\vec{r},\ \lambda)$ (cm^{-1}), and energy conversion efficiency from optical to thermal energy:

$$p_0(\vec{r},\ \lambda) = \Gamma \cdot F(\vec{r},\ \lambda) \cdot \mu_a(\vec{r},\ \lambda) \cdot \eta_{th}(\vec{r},\ \lambda),$$

where λ is the optical wavelength, $\vec{r}$ is the position of the optical absorber, and Γ is the Grüneisen parameter that depends on the type of medium. The propagation of the PA pressure wave $p(\vec{r},\ t)$ for a given wavelength λ can be described by the following wave equation [41, 42]

$$\left(\nabla^2 - \frac{1}{c^2}\frac{\partial^2}{\partial t^2}\right) p(\vec{r}, t) = -p_0(\vec{r})\frac{\mathrm{d}H(t)}{\mathrm{d}t},$$

where c is the speed of sound and $H(t)$ is the heating function defined as the thermal energy deposited per unit volume and unit time. Assuming thermal confinement, the heating function can be approximated as a

delta function. The solution to the wave equation is then expressed as follows.

$$p(\vec{r},t)=\frac{1}{4\pi c^2}\frac{\delta}{\delta t}\int\frac{p_0(\vec{r}')}{|\vec{r}-\vec{r}'|}\delta\left(t-\frac{|\vec{r}-\vec{r}'|}{c}\right)\mathrm{d}\vec{r}'.$$

For a perfect spherical target excited with uniform optical fluence, $p(\vec{r},\ t)$ would produce an N-shaped PA pulse with a width proportional to the diameter of the target [43, 44]. Any arbitrary volume can be described as a cluster of spherical targets, and thus, the PA pressure wave from any volumetric target can be estimated as a superposition of N-shaped pulses. The frequency of the PA wave is determined by the size and shape of the target, as well as the pulse width of the illumination. Large targets and long pulse widths generally generate more low-frequency components.

In the tomographic configuration of PAI, multiple US signal detectors (i.e. US transducers) receive the PA pressure wave at multiple positions to reconstruct a PA image describing the initial pressure, $p_0(\vec{r})$. One of the most commonly used reconstruction algorithms is back projection, analogous to conventional CT reconstruction, which utilizes the wave propagation delay based on distance between the target and each US detector [41]. The reconstructed PA initial pressure image using universal back projection is represented as:

$$p_0^R(\vec{r})=\frac{1}{\Omega_D}\int_{\Omega_D}b\left(\overrightarrow{r_D},t=\frac{|\vec{r}-\overrightarrow{r_D}|}{c}\right)\mathrm{d}\Omega_D,$$

where $b\left(\overrightarrow{r_D},t\right)=2\left\{p\left(\overrightarrow{r_D},t\right)-t\cdot\partial p\left(\overrightarrow{r_D},t\right)/\partial t\right\}$ is the back-projection term calculated from the PA pressure measured at the US detector location $\overrightarrow{r_D}$, $\mathrm{d}\Omega_D$ is the solid angle of the detector surface at $\overrightarrow{r_D}$ relative to the reconstruction point $\vec{r}$, and Ω_D is the total solid angle of all detectors. While universal back projection is theoretically exact, $p_0^R(\vec{r})$ may not be fully recovered due to heterogeneous chromophore distribution, heterogeneous optical fluence, acoustic attenuation (absorption or scattering), and imperfect transducer parameters (e.g. limited aperture and bandwidth).

Notably, the PA pressure amplitude depends on the optical fluence $F(\vec{r},\ \lambda)$, which tends to be diffusively distributed in biological tissues, significantly hindering the linearity of the PA amplitude with respect to the optical absorption of the target. Optical fluence is challenging to measure directly, but several estimation methods exist, such as Monte–Carlo photon transport simulations or PA image-based signal attenuation measurement techniques [43]. Assuming sufficient compensation for optical fluence and stable local temperature, the PA amplitude can be considered proportional to the optical absorption of the target at a given wavelength. This enables the differentiation of chromophores with unique optical absorption spectra. This process is also known as spectral unmixing, which estimates the concentration of each chromophore based on its known optical molar extinction coefficient $\in(\lambda)$ (i.e. optical absorption per unit molar concentration). Dominant biological chromophores in biomedical PAI include oxy-hemoglobin (HbO), deoxy-hemoglobin (HbR), melanin, lipid, and collagen. Notably, HbO and HbR are particularly important for assessing the functional status of suspicious thyroid nodules by estimating oxygen saturation (sO_2) or total hemoglobin concentration (HbT). For effective spectral unmixing, PAI should be performed at multiple wavelengths characteristic of each chromophore of interest. The number of wavelengths should exceed the number of chromophores to be distinguished. Let $\overline{p_0^R}(\vec{r},\lambda)=p_0^R(\vec{r},\lambda)/(\Gamma\eta_{\mathrm{th}}F(\vec{r},\lambda))$ represent the reconstructed PA initial pressure amplitude at position $\vec{r}$ and wavelength λ after full compensation for optical fluence and proportionality constants. Assuming the target consists solely of HbO and HbR, the collection of PA amplitude measurements at M wavelengths $(\lambda_1,\ \lambda_2,\ldots,\lambda_M)$ can be expressed as follows.

$$\begin{bmatrix}\overline{p_0^R}(\vec{r},\lambda_1)\\ \vdots\\ \overline{p_0^R}(\vec{r},\lambda_M)\end{bmatrix}=\begin{bmatrix}\in_{\mathrm{HbO}}(\lambda_1) & \in_{\mathrm{HbR}}(\lambda_1)\\ \vdots & \vdots\\ \in_{\mathrm{HbO}}(\lambda_M) & \in_{\mathrm{HbR}}(\lambda_M)\end{bmatrix}\begin{bmatrix}C_{\mathrm{HbO}}(\vec{r})\\ C_{\mathrm{HbR}}(\vec{r})\end{bmatrix},$$

where $\in_{\mathrm{HbO}}(\lambda)$, $\in_{\mathrm{HbR}}(\lambda)$, $C_{\mathrm{HbO}}(\vec{r})$, and $C_{\mathrm{HbR}}(\vec{r})$ are the molar extinction coefficients of HbO and HbR at wavelength λ and molar concentrations of HbO and HbR at position $\vec{r}$, respectively. The linear spectral unmixing process specifically calculates the estimated concentrations $\hat{C}_{\mathrm{HbO}}(\vec{r})$ and $\hat{C}_{\mathrm{HbR}}(\vec{r})$ by solving the least-squares problem, leading to a fixed solution

$$\begin{bmatrix}\hat{C}_{\mathrm{HbO}}(\vec{r})\\ \hat{C}_{\mathrm{HbR}}(\vec{r})\end{bmatrix}=\mathrm{pinv}\left(\begin{bmatrix}\in_{\mathrm{HbO}}(\lambda_1) & \in_{\mathrm{HbR}}(\lambda_1)\\ \vdots & \vdots\\ \in_{\mathrm{HbO}}(\lambda_M) & \in_{\mathrm{HbR}}(\lambda_M)\end{bmatrix}\right)\begin{bmatrix}\overline{p_0^R}(\vec{r},\lambda_1)\\ \vdots\\ \overline{p_0^R}(\vec{r},\lambda_M)\end{bmatrix},$$

where pinv(A) represents the pseudo-inverse of matrix A. This formula often provides overfitted results that produce negative concentrations; thus, a non-negativity constraint can be included in the least-squares problem. Using the estimated concentrations, HbT and sO_2 were calculated as:

$$\hat{C}_{\mathrm{HbT}}(\vec{r}) = \hat{C}_{\mathrm{HbO}}(\vec{r}) + \hat{C}_{\mathrm{HbR}}(\vec{r}),$$

$$\mathrm{sO}_2(\vec{r}) = \frac{\hat{C}_{\mathrm{HbO}}(\vec{r})}{\hat{C}_{\mathrm{HbT}}(\vec{r})} \times 100\,[\%].$$

In contrast to conventional USI, which relies on transmitting US waves into target tissue and detecting reflected waves (pulse-echo imaging), PAI generates acoustic PA waves instantaneously through light absorption in the tissue. The system detects these waves as they propagate from the target, making PAI fundamentally distinct in terms of signal generation. A typical PAI system consists of a pulse illumination source, such as a crystal laser, laser diode, or light-emitting diode, and an US signal acquisition system equipped with US transducers in various configurations (e.g. single-element or array transducers). For clinical thyroid imaging, PAI commonly utilizes conventional linear-array US transducers capable of dual-modal PAI/USI or curved-array transducers specifically for PAI-based tomographic imaging. The illumination sources used for thyroid imaging typically operate at pulse repetition frequencies (PRFs) between 10 and 50 Hz with high pulse energies ($\sim$100 mJ), providing rapid wavelength switching in the near-infrared range (700–1000 nm), critical for functional PA measurements. To accomodate handheld scanning, flexible optical fiber bundles or diffusive optics attached to US transducers through customized probe adapters. In most thyroid PAI studies, US transducers operate at frequencies between 5 and 10 MHz, ensuring that the laser pulse width is approximately aligned with the inverse of the US frequency ($<$100 ns). In the case of red blood cells, approximately modeled as spherical targets, their PA signal from dense clusters inside the blood vessels can be modeled as the summation of N-shaped PA pulses. Thus, blood vessels generate sharp amplitude changes (high frequencies) near vessel walls and more gradual changes (low frequencies) in the vessel lumen. Large vessels, such as the common carotid artery and internal jugular veins, are likely to produce low-frequency components ($<$1 MHz) which can be degraded during detection with conventional US transducers. Conversely, small vessels generate higher-frequency components, which are less affected by the limited bandwidth of clinical US transducers. Thus, PAI can effectively depict small thyroid vasculature and analyze abnormal vascular patterns near suspicious nodules or assess functional metrics like sO_2 and HbT (figure 1, left).

2.2. Principles of UFD imaging

UFD imaging is an US Doppler technique that utilizes fast plane-wave-based image acquisition with an improved clutter rejection technique. In contrast to conventional US B-mode or Doppler imaging which uses focused US waves to concentrate acoustic energy along specific scan lines, UFD employs simultaneous emissions of US waves across all elements in an array transducer, creating a planar wavefront that scans the entire field of view (FOV) with a single transmission. This method achieves ultrafast frame rates, reaching several thousand frames per second (fps), which facilitates the detailed observation of slow-motion dynamics within tissues. Traditional focused USI achieves a high signal-to-noise ratio (SNR) by repeatedly emitting focused US pulses at specific scan lines, but this process requires hundreds of emissions, limiting frame acquisition rates to tens of fps. By emitting a plane-wave across the entire transducer array, UFD eliminates the need for repeated focused emissions, drastically increasing the frame rate. However, a single plane-wave US emission can suffer from reduced SNR and contrast due to dispersed acoustic power, simultaneous tissue excitation, and transducer element crosstalk. To mitigate these issues, UFD employs multiple plane-wave emissions with stepwise angular steering. The resulting US images from various steering angles are then coherently compounded, where the phase information is preserved and summed. This approach enhances the SNR and image quality compared to single plane-wave emissions, although the frame rate is reduced accordingly compared to the fastest single plane-wave method. Nonetheless, the frame rate remains significantly higher than that of conventional focused USI.

Conventional US Doppler images are generated through clutter filtering (i.e. removing unnecessary tissue signals) applied to an ensemble set of IQ-demodulated US image frames, obtained via scanline acquisition [45]. Each scanline in the FOV is insonified with multiple pulse-echo sequences, typically ranging from 5–15 pulses, using a uniform PRF to form an ensemble packet. These scanline signals are beamformed, IQ-demodulated, and clutter-filtered along the ensemble axis to remove tissue pixels that exhibit relatively slow motion compared to vascular flow. The clutter-filtered IQ signals are expressed as complex numbers, containing two types of vascular flow information: magnitude (related to power) and phase (related to velocity). Power Doppler images are reconstructed by summing the magnitudes of all IQ

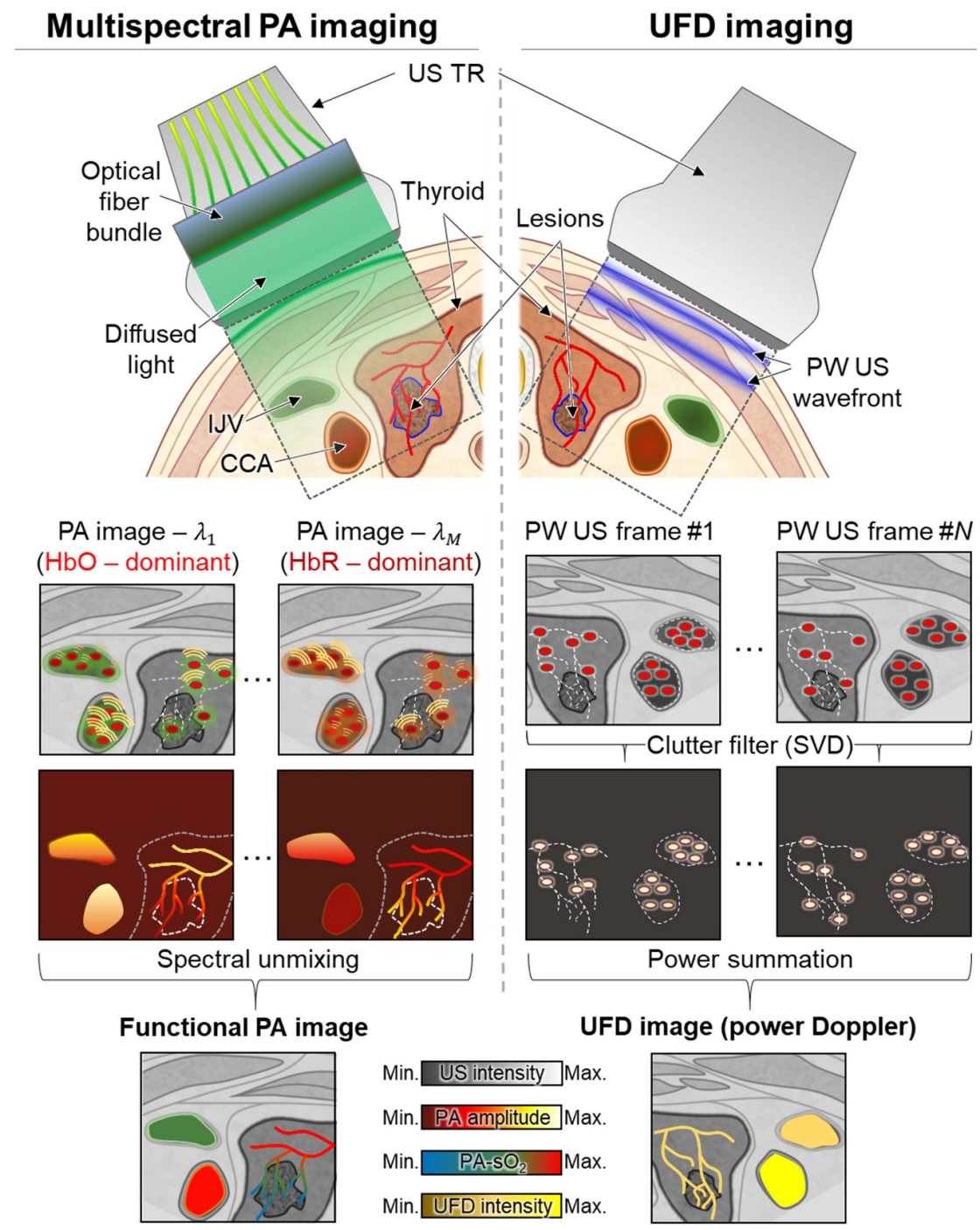

Figure 1. Conceptual schematics for PA and UFD imaging techniques for thyroid cancer diagnosis. US TR, ultrasound transducer; IJV, internal jugular vein; CCA, common carotid artery; Tr, trachea; Es, esophagus; PW, plane-wave; US, ultrasound; PA, photoacoustic; λ_m, mth optical wavelength; HbO, oxy-hemoglobin; HbR, deoxy-hemoglobin; SVD, singular value decomposition; sO_2, hemoglobin oxygen saturation; UFD, ultrafast Doppler.

signals, allowing visualization of vascular structures based on flow intensity. More quantitatively, spectral Doppler and color Doppler modes utilize the phase information to measure flow velocity, which is based on the Doppler frequency shift (f_D)

$$f_D = \frac{2 \cdot f_c \cdot v \cdot \cos\theta}{c},$$

where f_c is the center frequency, v is the flow velocity, c is the speed of sound in the medium, and θ is the angle between the flow direction and the US transducer. The maximum measureable flow velocity is limited

by the PRF according to the Nyquist sampling theorem

$$\mathrm{PRF} \geqslant 2 \cdot f_{\mathrm{D,\,max}} = \frac{4 \cdot f_c \cdot v_{\max} \cdot \cos\theta}{c}.$$

The Doppler frequency shift is typically estimated using autocorrelation techniques, such as the lag-1 autocorrelation-based phase-shift measurement between two consecutive IQ scanline signals. Spectral Doppler provides a plot of the temporal variation of blood flow in a small sample gate region, while color Doppler generates an image that maps flow velocity across the FOV using a red-to-blue colormap.

Based on its fast frame rate and ability to scan the entire view, advanced clutter filtering using singular value decomposition (SVD) can be applied to plane-wave US images to detect speckle signals flowing inside small vessels [46]. Let us assume a set of coherently compounded plane-wave US images acquired in the dimensions $N_z \times N_x \times N_t$, where N_z and N_x represent the number of pixels of each US image in the axial and lateral dimensions, respectively, and N_t denotes the number of ensemble image frames captured at different times. Conventional clutter filtering is performed using high-pass filtering along the temporal axis (in the N_t direction) for each pixel in the $N_z \times N_x$ grid, assuming that speckle signals from flowing vessels vary faster than tissue signals. However, SVD filtering offers a spatiotemporal filtering that simultaneously considers the spatial correlation of $N_z \times N_x$ pixels and the temporal variation of N_t pixels. The SVD decomposes the image into principal components (i.e. eigenvectors or eigenimages) ranked by significance, from common tissue structures to random noise, based on their corresponding singular values. The high-value singular vectors (representing tissue structures) and low-value vectors (representing noise) are filtered out by zeroing the respective singular values, and the remaining signals are power-summed to generate a power Doppler image depicting small vasculature (figure 1, right). To perform SVD on the three-dimensional (3D) $N_z \times N_x \times N_t$ US image data $s(z,x,t)$, each US image is reshaped from a two-dimensional (2D) $N_z \times N_x$ matrix into a $(N_z \cdot N_x) \times 1$ column vector and combined into a $(N_z \cdot N_x) \times N_t$ Casorati matrix $S(w,t)$. SVD is then performed on $S(w,t)$ to obtain the spatial (U) and temporal (V) eigenvector matrices and the singular value matrix Λ, such that $S = U\Lambda V^H$. Here, each column of U and V represents the spatial and temporal eigenvectors, respectively, and Λ is a diagonal matrix containing the singular values in descending order. Slowly-varying tissue signals (clutter) are found in the lower ranks. Clutter filtering can be achieved by zeroing the first diagonal values of Λ up to a cutoff rank r_{clutter}, and reconstructing $\hat{S} = U\hat{\Lambda}V^H$, where $\hat{\Lambda} = \Lambda$, $\hat{\Lambda}\ (i,\ i) = 0$ for $i \leqslant r_{\mathrm{clutter}}$. Additionally, noise components can be reduced by putting $\hat{\Lambda}\ (i,\ i) = 0$ for $i \geqslant r_{\mathrm{noise}}$. A UFD image $I_{\mathrm{UFD}}(z,x)$ is then generated by reshaping the $(N_z \cdot N_x) \times N_t$ matrix $\hat{S}$ back to $N_z \times N_x \times N_t$ matrix $\hat{s}$ and performing a power summation along the temporal axis:

$$I_{\mathrm{UFD}}(z,x) = \sum_{t=1}^{N_t} |\hat{s}(z,x,t)|^2.$$

The number of ensemble frames (N_t) determines the number of decomposed eigenvectors, and thus, more frames allow more sensitive clutter removal, though at the cost of increased acquisition time.

Typically, when conventional linear array transducers are used for thyroid imaging, coherently compounded plane-wave US images are acquired at 500–1000 fps, and approximately 200–500 frames are collected for SVD filtering. The cutoff value for SVD filtering is usually selected manually and often corresponds to the elbow point in the singular value plot (in descending order) or the transition point in the correlation matrix of the spatial eigenvectors U [46]. In UFD images, the deeper regions may exhibit increased noise due to time-gain compensation applied during US data acquisition. The depth-dependent noise level can be measured either directly from the US acquisition system (with transmission off) or from the last singular vector in the SVD decomposition. Afterward, the original UFD image is compensated by adjusting for the estimated noise level to equalize the noise, improving vessel signal visualization through a single threshold value [47].

2.3. Major features of PAI and UFD imaging

PAI measures optical absorber distributions to provide molecular information, using pulse laser illumination and ultrasonic detection. PAI mainly detects HbO and HbR in the red blood cells using NIR wavelengths, which are used to describe the formation of vasculature near suspicious lesions. The visibility of vascular structure, however, may not be definite for PAI due to practical factors such as low SNR of PA signals, limited detection aperture or limited bandwidth of conventional array transducers. The major strength of PAI comes from the capability of quantifying the concentration of HbO and HbR separately using spectral unmixing of multi-wavelength PAI data. Thanks to this feature, PAI is able to present clinically viable biomarkers such as sO_2 for evaluating malignancy of thyroid nodules. PAI acquisition time depends on the number of optical

Table 1. Summary of major characteristics of PAI and UFD for thyroid diagnosis. PA; photoacoustic; US, ultrasound; PAI, PA imaging; UFD, ultrafast Doppler; PW, plane-wave; HbO, oxy-hemoglobin; HbR, deoxy-hemoglobin; HbT, total hemoglobin; sO_2, hemoglobin oxygen saturation; N_λ, number of optical wavelengths; N_{acq}, number of acquisitions per frame; N_a, number of steer angles; N_t, number of ensemble frames; PRF, pulse repetition frequency.

Modality	Transmission	Reception	Source of contrast	Image acquisition time	Major diagnostic information
PAI	Pulse laser (N_λ wavelengths)	PA signal	Optical absorbers (HbO, HbR, lipid, water, collagen)	$N_\lambda \cdot N_{acq}$ /Laser PRF	Quantitative molecular information (e.g. HbT, sO_2)
UFD	PW US (N_a steer angles)	Reflected US signal	Blood flow	$N_a \cdot N_t$ /US PRF	Vascular morphologyand flow intensity

wavelengths, number of acquisitions per PA image, and PRF of laser source, typically around 0.2–0.5 s per a set of multi-wavelength PAI frames.

UFD detects changes in US speckle signals caused by blood flow, revealing the morphology of microvessels. UFD detects the thyroid vasculature sensitively and with high spatial resolution, using the ultrafast plane-wave acquisition and spatio-temporal SVD clutter filtering. Yet, UFD lacks quantitative functional information compared to PAI, and high computational power is required to support ultrafast plane-wave image acquisition and to perform SVD on heavy spatio-temporal ensemble data. For UFD, acquisition time is determined by the number of steer angles, number of ensemble frames, and the PRF of plane-wave US images. While the PRF of plane-wave US is generally tens to hundreds times faster than the PRF of lasers, a single UFD frame requires N_t frames, sometimes up to several hundred. Therefore, the overall acquisition time for both modalities is similar, around 0.5 s typically. Table 1 summarizes key features of PAI and UFD in thyroid diagnosis.

3. PAI for assessing malignancy of thyroid nodules

Based on these principles, PAI can visualize the optical absorption characteristics of tissues, thereby providing information on the molecular composition of biological samples [48, 49]. Although various exogenous contrast agents have been widely investigated for contrast-enhanced PAI [50–54], their application in human studies presents significant challenges. Consequently, clinical applications of PAI typically rely on intrinsic chromophores, particularly HbO and HbR, to provide functional information [55, 56]. To complement the relatively limited structural information, PA images are often combined with simultaneously acquired US images [57–59]. PAI has been applied to the study of various cancers, including breast [60–62], skin [63–65], and prostate cancers [66–68]. This section focuses on thyroid cancer studies, including *ex vivo* and *in vivo* human thyroid samples. The specific characteristics of the reviewed PAI studies on thyroid nodules are summarized in table 2.

Early studies assessed the feasibility of multispectral PA analysis using extracted thyroid tissues. For instance, Kang *et al* investigated the use of PA imaging to detect microcalcifications, a feature often associated with tumors, in excised thyroid tissues [69]. In their study, thyroid samples were collected from patients scheduled for surgery. After surgical resection, the samples underwent radiography to determine their suitability for PA analysis. Consequently, 36 tissues samples from 18 patients were included in the PA analysis. The PA images were acquired at an excitation wavelength of 700 nm using the PAI system (figure 2(a)). However, the resulting PA images did not adequately reveal the presence of microcalcifications, as confirmed by radiography (figure 2(b)). This study was limited to single-wavelength PAI, and thus, multispectral analysis was not feasible.

Dogra *et al* reported the feasibility of multispectral PAI for differentiating thyroid nodules by analyzing the HbO and HbR components in resected tumor samples [70]. They recruited 50 patients who underwent thyroidectomy or lobectomy, collecting 88 thyroid sections comprising excised tissues. Multispectral PA images were obtained at wavelengths of 760, 850, 930, and 970 nm, corresponding to HbR, HbO, lipid, and water, respectively. The results showed significant differences between malignant and non-malignant nodules (benign, colloid, and normal), particularly in mean HbR intensity. Statistical analysis using a logistic regression model showed promising classification accuracy, with a sensitivity of 69.2% and specificity of 96.9% for distinguishing malignant from non-malignant samples. In a subsequent study, they expanded their method to the frequency domain of PA signals and explored the classification potential of malignant and normal tissues [71]. In this study, 65 thyroid sections were collected from 50 patients, and multispectral PA data were acquired at wavelengths of 760, 800, and 850 nm (figure 2(c)). In addition to the PA values, the signals were transformed into the frequency domain, where three parameters (slope, mid-band fit, and

Table 2. Summary of representative studies on PA analysis of thyroid nodules. PA, photoacoustic; US, ultrasound; PRF, pulse repetition frequency; λ, optical wavelength; f_c, central frequency range; n_e, number of elements; Se, sensitivity; Sp, specificity; HbO, oxy-hemoglobin; HbR, deoxy-hemoglobin; sO_2, hemoglobin oxygen saturation level; GD, Graves' disease; PTC, papillary thyroid cancer; Ref, reference.

			Laser		US transducer			Accuracy		
Method	Sample	Parameters	PRF [Hz]	λ [nm]	Geometry	f_c [MHz]	n_e	Se [%]	Sp [%]	References (Year)
ex vivo	36 resected tissues from 18 patients	Microcalcifications	10	700	Linear	5–12	128	—	—	[69] (2014)
	88 resected sections from 50 patients	HbO, lipid, water	10	760, 850, 930, 970	Linear	2.4–7.4	32	69.2	96.9	[70] (2014)
	65 resected sections from 50 patients	slope, mid-band fit, intercept in frequency domain	10	760, 800, 850	Linear	2.4–7.4	32	—	—	[71] (2017)
in vivo	2 healthy volunteers	Vasculature	10	800	Arc-shaped	–7.5	64	—	—	[72] (2016)
	3 healthy volunteers, 10 PTC patients	Vasculature	10	1064	Linear	3–9	192	—	—	[73] (2017)
	8 normal, 6 GD, 13 benign, 3 PTC lobes from 13 patients and 3 healthy volunteers	HbO, HbR, sO_2, fat, water	25	700, 730, 760, 800, 850, 900, 920, 950	Arc-shaped	3	256	—	—	[74] (2019)
	16 benign, 11 PTC nodules from 27 patients	HbO, HbR, lipids, water, collagen	25	680, 700, 730, 760, 800, 850, 900, 930, 970, 1000, 1030, 1064, 1100, 1195	Arc-shaped	3.5	256	—	—	[75] (2023)
	29 benign, 23 PTC nodules from 52 patients	sO_2, sO_2 distribution, PA spectral gradient	10	700, 756, 796, 866, 900	Linear	3–12	128	83	93	[76] (2021)

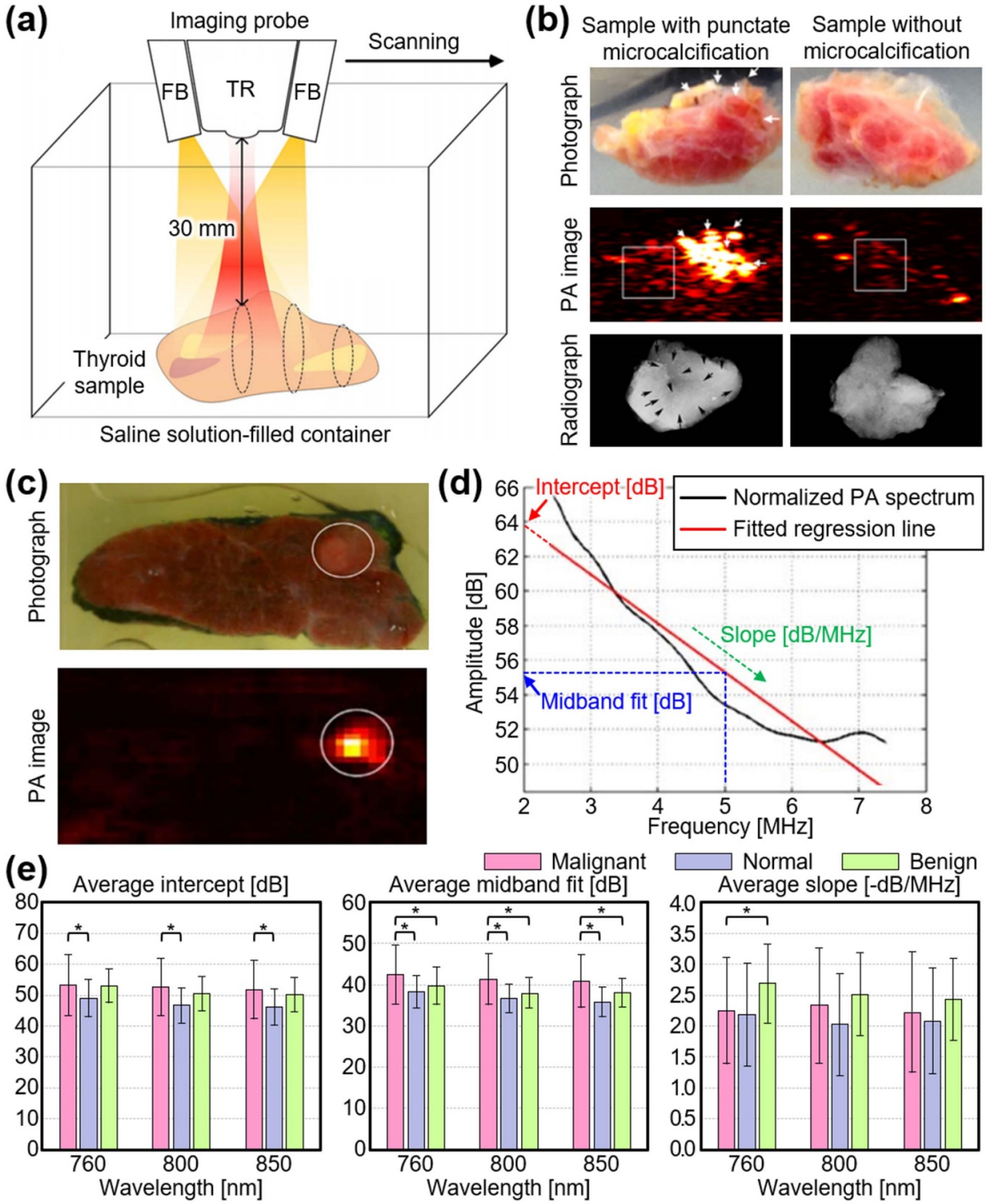

Figure 2. Representative PA analyses of extracted thyroid tissues. (a) Experimental setup for PA imaging of thyroid tissues *ex vivo*. (b) Photograph, PA image, and radiograph of samples with punctate microcalcification and without calcification. Saturated PA signals from blood coagulations (white arrows) were excluded from the analysis. ROIs for microcalcification analysis are indicated by white boxes, selected where compact punctate calcifications were confirmed in the corresponding radiograph (black arrows). (c) Photograph and resulting PA images of the sliced thyroid sample. ROIs (white circles) of malignant, benign, and normal tissues were designated for spectral PA analyses. (d) Representative PA spectrum in the frequency domain with a fitted regression line for quantifying three spectral parameters: intercept, mid-band fit, and slope. (e) Average values of the spectral parameters. PA, photoacoustic; ROI, region of interest; TR, ultrasound transducer; FB, fiber bundle; $^{*}P < 0.05$. (a) and (b) Reproduced from [69]. CC BY 4.0. (c)–(e) [71] John Wiley & Sons. © 2017 by the American Institute of Ultrasound in Medicine.

intercept) were quantified at each wavelength (figure 2(d)). Among the nine total parameters analyzed in the frequency domain, six parameters related to the mid-band fit and intercept successfully differentiated malignant from normal thyroid tissues (figure 2(e)). Although the parameters were analyzed separately and no comprehensive statistical analysis was provided, the results suggest a promising potential for PA analysis in detecting malignancy. However, *ex vivo* quantification of HbR and HbO levels is influenced by rapid postmortem deoxygenation, progressive blood loss, and freezing-thawing artifacts, all of which alter tissue optical properties. These limitations highlight the necessity for *in vivo* validation, where physiological conditions are preserved.

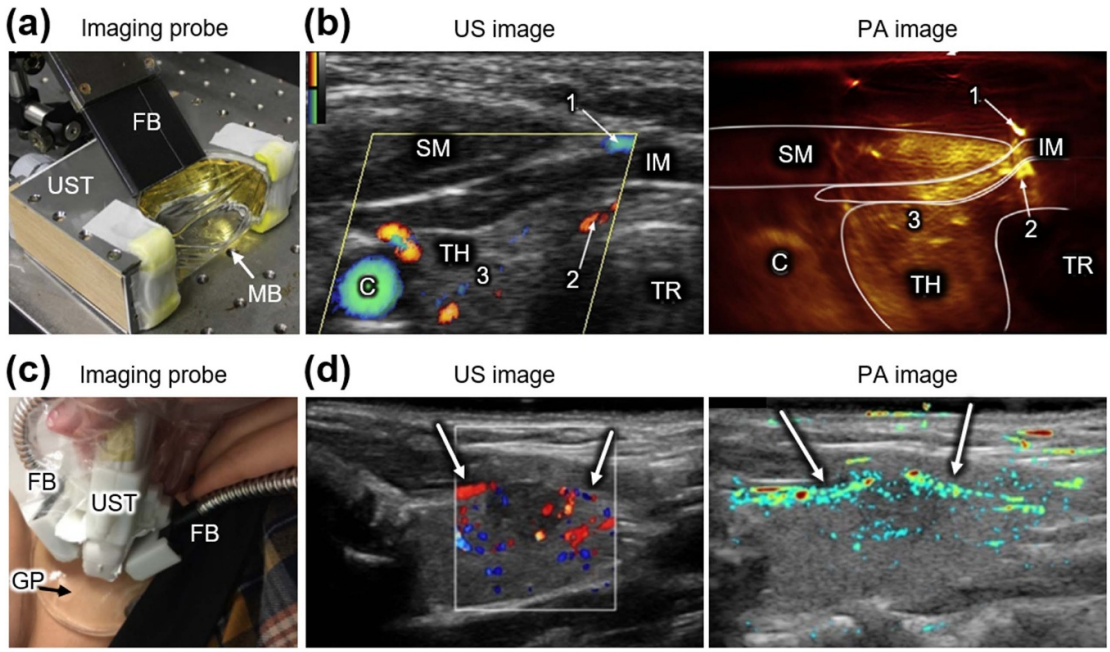

Figure 3. Representative dual-modal US and PA probe for *in vivo* human imaging. (a) The photograph of a PA imaging probe comprises a curved array transducer. (b) US and PA images of thyroid region in a healthy volunteer. US B-mode (gray-scale) and color Doppler (pseudo-color) images are overlaid. Numbers represent blood vessels in the thyroid. (c) Photograph of a PA imaging probe comprises a linear array transducer. (b) US and PA images of the thyroid region in a healthy volunteer. US B-mode (gray-scale) and color Doppler (pseudo-color from blue to red) images are overlaid. US B-mode (gray-scale) and PA (pseudo-color from green to red) images are overlaid. Feeding blood vessels are indicated with white arrows. US, ultrasound; PA, photoacoustic; UST, ultrasound transducer; FB, fiber bundle; GP, gel pad; MB, membrane; SM, sternocleidomastoid muscle; IM, infrahyoid muscle; C, carotid artery; TH, thyroid lobe; TR, Trachea. (a) and (b) Reproduced from [72]. CC BY 4.0. (c) and (d) Reproduced with permission from [73].

Building on the previously validated feasibility of PA analysis for thyroid malignancies, efforts have progressed to acquire PA images from *in vivo* human subjects. Dima and Ntziachristos developed a PAI system specifically designed for *in vivo* human thyroid imaging [72]. They designed a handheld probe equipped with an arc-shaped transducer and a custom-designed optical fiber bundle (figure 3(a)). The transducer comprised 64 piezoelectric elements arranged with a radius of 40 mm and an angular span of 172°. To facilitate the effective delivery of PA waves, the cavity within the arc-shaped array was filled with deionized water and sealed with a membrane. The feasibility of the probe was validated by acquiring PA images from two healthy female volunteers. PA images obtained at a wavelength of 800 nm were compared with corresponding B-mode and color Doppler US images, confirming the vascular analysis capability of PAI (figure 3(b)). The results demonstrate the potential of *in vivo* PAI for outlining thyroid and vascular features at a depth of approximately 20 mm below the skin. Yang *et al* introduced a more compact hand-held probe by integrating a 192-element linear array transducer with a bifurcated fiber bundle (figure 3(c)) [73]. They initially verified the imaging capability of their system using three healthy volunteers and then obtained PA and US images from 10 patients diagnosed with papillary thyroid cancer (PTC) nodules. Despite using a single wavelength of 1064 nm, the PAI system successfully detected small blood vessels within thyroid tissues, which are typically challenging to visualize using conventional color Doppler USI (figure 3(d)). These initial clinical trials in humans demonstrated the significant potential of PAI to provide information complementary to conventional ultrasonography. Based on these findings, subsequent studies have conducted multispectral PA analysis in human thyroids *in vivo*.

Roll *et al* conducted a pilot study utilizing multispectral PA analysis to assess the molecular composition of thyroid lobes, focusing on HbO, HbR, fat, and water through a spectral unmixing technique [74]. They recruited 13 patients, including three with Graves' disease, nine with benign disease, and three with PTC, alongside three healthy volunteers. This study used a previously developed multispectral PAI system equipped with a 256-element arc-shaped array [77]. Multispectral PA images were obtained at wavelengths of 700, 730, 760, 800, 850, 900, 920, and 950 nm (figure 4(a)), and the spectrally unmixed values were compared (figure 4(b)). The results revealed significant differences between lobes affected by Graves' disease and healthy lobes, with notably higher levels of HbR ($P = 0.0055$), higher HbT ($P = 0.0084$), and lower fat content ($P = 0.0293$). In addition, PTC nodules exhibited lower sO_2 levels ($P = 0.0393$) and fewer fat components ($P = 0.1295$) compared to benign nodules. More recently, Noltes *et al* employed the same

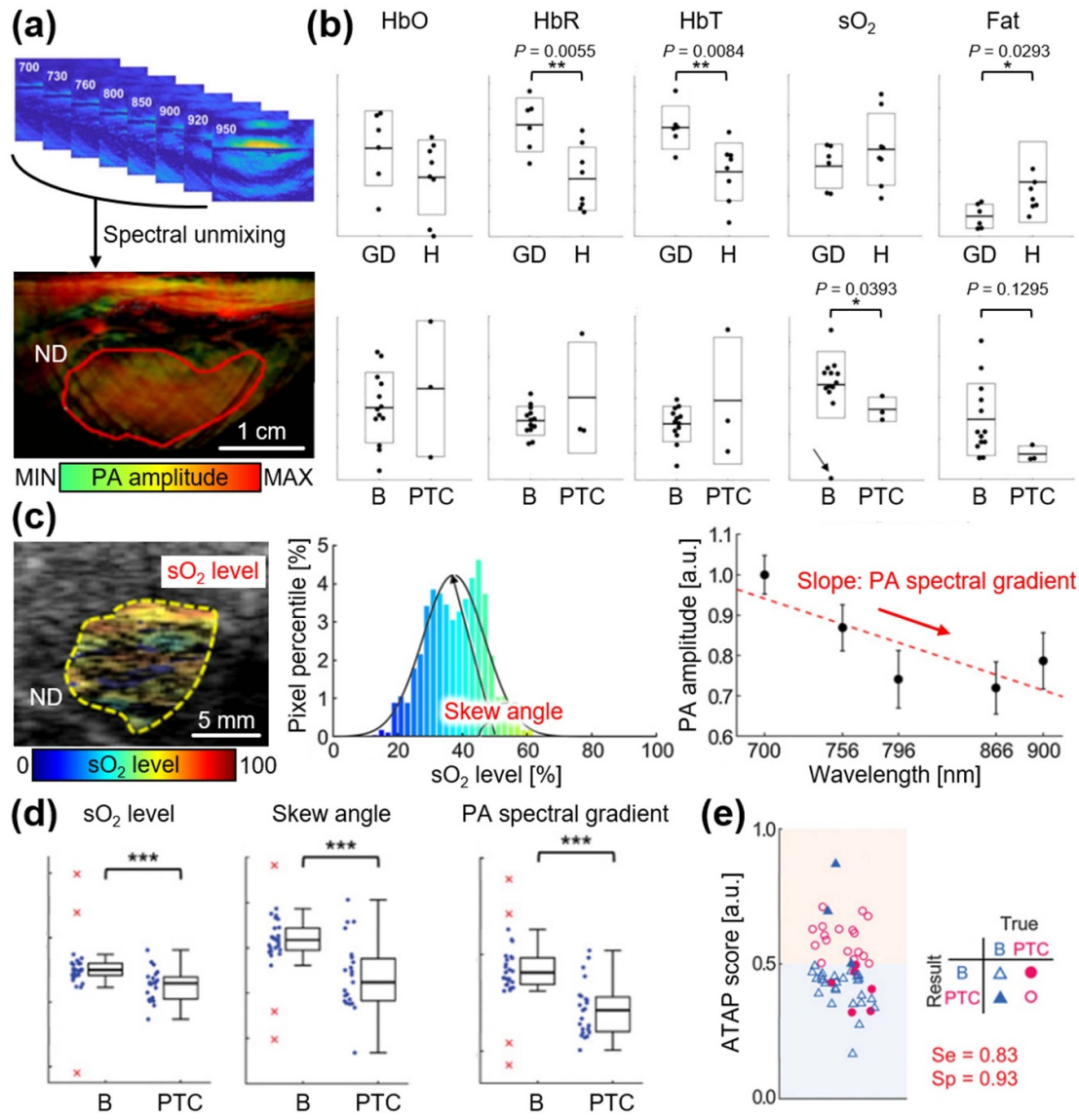

Figure 4. Representative multispectral PA analyses of human thyroid *in vivo*. (a) Multispectral PA images and spectrally unmixed images in thyroid nodule area. (b) Statistical comparison between Graves' disease and healthy tissue (upper row), and between benign and PTC tissue (lower row). (c) The parameters for multispectral PA analysis of thyroid nodules *in vivo*. (d) Statistical comparison between benign and PTC nodules with the multispectral parameters. (e) Classification accuracy of the proposed scoring method. The red area denotes the decision region of PTC, while the blue area denotes the decision region of benign. PA, photoacoustic; HbO, oxy-hemoglobin; HbR, deoxy-hemoglobin; HbT, total hemoglobin; sO_2, hemoglobin oxygen saturation; GD, Graves' disease; H, healthy; B, benign; PTC, papillary thyroid cancer; ND, thyroid nodule; ATAP, the American Thyroid Association and the photoacoustic probability of PTC; Se, sensitivity; Sp, specificity. $^{*}P < 0.05$, $^{**}P < 0.01$, $^{***}P < 0.001$. (a) and (b) Reproduced with permission from [74]. (c)–(e) Reproduced with permission from [76].

system to investigate vascularity in thyroid lobes across a broader range of wavelengths [75]. They recruited 27 patients (16 with benign conditions and 11 with PTC) and obtained multispectral PA images at wavelengths of 680, 700, 730, 760, 800, 850, 900, 930, 970, 1000, 1030, 1064, 1100, and 1195 nm. This approach allowed for the visualization of specific components such as HbO, HbR, lipids, and water. By comparing the resulting images with histopathological sections, they verified that PAI could resolve small blood vessels with diameters of approximately 250 μm at depths of up to 2 cm. Although multispectral analysis demonstrated significant potential for visualizing and analyzing molecular components in thyroid lobes, the study was limited by a relatively small sample size, which constrained the statistical analysis.

Kim *et al* introduced a multiparametric approach for analyzing thyroid nodules and proposed a novel scoring method to differentiate between malignant and benign nodules [76]. They recruited 52 patients comprising 29 with benign nodules and 23 with PTC, and acquired multispectral PA images at wavelengths of 700, 756, 796, 866, and 900 nm using a previously reported PA and USI system equipped with a 128-element linear array transducer and a portable pulsed laser (figure 4(c)) [78]. From the multispectral PA data, they quantified three parameters related to the HbO and HbR components: the mean sO_2 level, skew angle of the

sO_2 distribution within the nodule, and spectral gradient of the PA signal (figure 4(d)). Using a support vector machine technique, they developed a decision function integrated with conventional US-based risk stratification to propose this novel scoring method. This new approach demonstrated an ability to differentiate malignant nodules from benign ones with sensitivity of 83% and specificity of 93%, showing significant promise in addressing the low specificity often associated with current US-based techniques

4. Ultrafast US Doppler imaging for assessment of thyroid vascularity

Doppler US has been explored as a tool to differentiate between malignant and benign nodules by assessing intranodular vascularity [79–81]. However, these studies have not demonstrated a clear correlation between vascularity and malignancy [24], primarily due to the limitations of conventional Doppler methods, which often struggle to accurately detect low-velocity blood flow. To address this limitation, microvascular imaging has been developed, capable of detecting low-velocity microvessels by incorporating low-frequency components in Doppler processing. Several studies have demonstrated that advanced microvascular imaging can significantly enhance the diagnostic accuracy for thyroid cancer by assessing the microvasculature within nodules [82–84]. Recently, UFD imaging has emerged as a promising technique for visualizing vasculature, offering significant advantages including higher frame rates and improved detection of slow blood flow [85–87]. UFD imaging holds great potential for enhancing diagnostic accuracy across various clinical applications, particularly in visualizing microvascular features [88, 89]. This section explores UFD imaging techniques for investigating the vascularity of thyroid nodules, with key findings summarized in table 3.

Bercoff *et al* introduced an ultrafast plane-wave US compounding technique to enable rapid data acquisition for Doppler imaging [90]. This method produces high-resolution US images by transmitting multiple plane-waves at various angles into the medium and summing the backscattered signals. Using nine different angles, UFD images were generated at a frame rate of 1600 Hz, which is up to 16 times faster than traditional focused US imaging. This increased frame rate allows for the detection of weak signals within tissues, significantly improving the sensitivity of microvasculature detection. To evaluate the performance of the ultrafast compounding technique, UFD images of the thyroid regions in healthy volunteers were acquired. Findings indicated that UFD imaging provides clearer visualization of microvessels compared to conventional Doppler techniques, highlighting its promise for disease detection through microvascular network analysis.

Visualization of small-vessel blood flow can be improved by exploiting the spatiotemporal characteristics of Doppler ensembles. Specifically, applying SVD filtering and selecting appropriate ranks can effectively suppress clutter signals. To address the challenges of accurately determining the blood flow subspace boundary during SVD filtering, Baranger *et al* proposed an efficient estimator for automatic subspace thresholding [91]. They evaluated the performance of this estimator against 13 other potential methods, focusing on various characteristics of SVD components, such as singular values, temporal singular vectors, and spatial singular vectors. The results demonstrate the superior performance of the proposed method and highlight the robustness and efficacy of the spatial similarity matrix, which relates to the correlation between spatial singular vectors. UFD images of the thyroid region obtained from a healthy volunteer confirmed that automated SVD filtering improved the contrast-to-noise ratio (CNR), effectively suppressing clutter and enhancing image quality.

One key challenge in thyroid imaging is compensating for physiological motion, particularly from the pulsating carotid artery. Nayak *et al* introduced a spatiotemporal filtering method that corrects tissue motion before SVD filtering, thereby improving tissue coherence [92]. They employed a 2D normalized cross-correlation (2D-NCC) method to estimate axial and lateral displacements in each US frame, subsequently globally shifting the images to align with the first frame. To validate the feasibility of their motion correction algorithm, UFD images were acquired from a patient with a suspected malignant nodule. Compared to conventional UFD images with global SVD filtering, the proposed method produced clearer visualizations of small blood vessels, demonstrating the promising feasibility of the motion correction algorithm. Furthermore, the CNR of blood vessels increased to 8.17 dB in the motion-corrected UFD image, compared to 0.87 dB in the conventional UFD image. This indicates that the 2D-NCC method effectively suppresses background noise by correcting motion artifacts. However, this technique is limited to tracking and correcting in-plane motion. Therefore, the authors hypothesized that longitudinal imaging of the thyroid gland would be more reliable than transverse imaging due to the natural anatomical orientation of the rigid trachea. In a subsequent study, they evaluated imaging performance in both the longitudinal and transverse planes using the same 2D-NCC method [93]. A total of 24 patients with suspicious thyroid nodules were recruited, and compounded plane-wave US images were acquired (figure 5(a)). The average cross-correlation coefficient of the US images was significantly higher in the longitudinal plane than in the transverse plane, indicating the presence of out-of-plane motion associated with carotid pulsation

Table 3. Summary of representative studies on the vascularity analysis of thyroid nodules using UFD imaging. UFD, ultrafast Doppler; f_c, central frequency range; n_e, number of elements; θ_s, steering angle.

	US transducer			UFD imaging				
Sample	Geometry	f_c [MHz]	n_e	Imaging depth [mm]	Frame rate [Hz]	Number of θ_s	Maximum θ_s [deg]	References (Year)
1 healthy volunteer	Linear	8	256	25	1600	9	9	[90] (2011)
1 healthy volunteer	Linear	2–10	192	25	1443	11	5	[91] (2018)
1 supicious malignant	Linear	3–12	128	35	616	7	3	[92] (2019)
24 supicious malignants	Linear	3–12	128	35	616	7	3	[93] (2020)
15 supicious malignants	Linear	3–12	128	35	600–700	7	3	[94] (2021)
1 healthy volunteer	2D matrix	3	32×32	30	572	9	2[a]	[95] (2015)
1 healthy volunteer	2D row-column	3	$128 + 128$	35	441	22	6[a]	[96] (2024)

[a] Angles in both lateral directions.

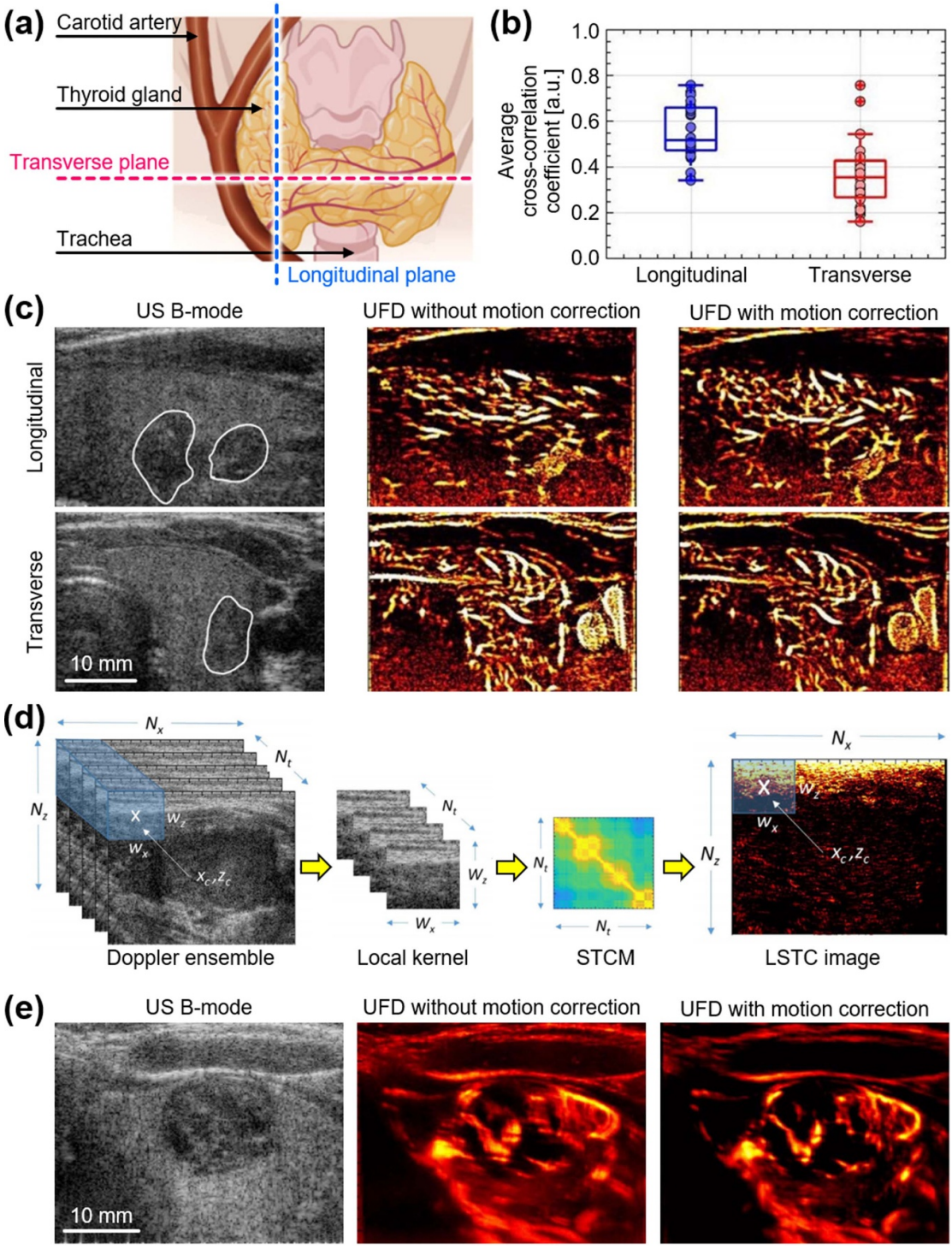

Figure 5. Representative motion-corrected UFD images of human thyroids *in vivo*. (a) Schematic of the anatomical position of the thyroid gland with respect to the longitudinal and transverse planes. (b) US B-mode and corresponding UFD images of the thyroid region at the longitudinal and transverse planes. White boundaries in B-mode images indicate the malignant nodules. (c) Schematic illustration for the LSTC motion correction process. *x*, *z*, *t*, correspond to axial, lateral, and temporal coordinates, respectively. (d) *In vivo* thyroid images with corresponding microvascular blood flow with and without LSTC motion correction. UFD, ultrafast Doppler; US, ultrasound; STCM, spatiotemporal correlation matrix; LSTC, local spatiotemporal correlation. (a)–(c) Reproduced from [93]. CC BY 4.0. (d) and (e) [94] John Wiley & Sons. © 2021 The Authors. Medical Physics published by Wiley Periodicals LLC on behalf of American Association of Physicists in Medicine.

(figure 5(b)). In the resulting UFD images (figure 5(c)), the SNR and CNR values were compared to assess image quality, revealing superior values in the longitudinal view (12.95 ± 3.76 dB for SNR and 16.48 ± 4.60 dB for CNR) compared to the transverse view (3.72 ± 0.89 dB for SNR and 6.22 ± 1.69 dB for CNR). These results indicate that carotid pulsation can be effectively corrected using the 2D-NCC method in a longitudinal view. The motion correction algorithm was further improved by incorporating local

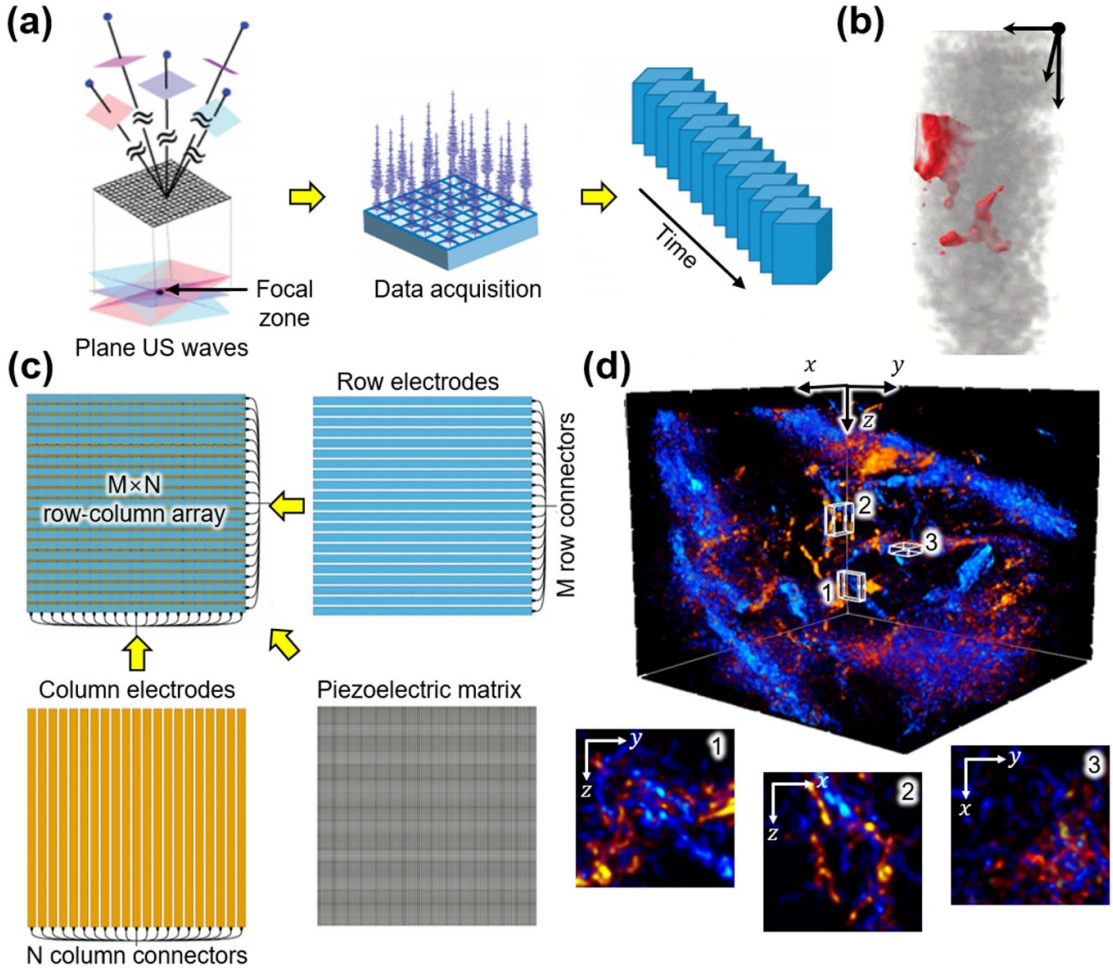

Figure 6. Representative volumetric UFD images of human thyroids *in vivo*. (a) Schematic of the 3D volume formation by compounding multiple tilted planewaves with varying propagation angles. (b) 3D UFD image of the human thyroid. Red denotes the blood flow. (c) Schematic of the configuration of the row-column array transducer. (d) 3D UFD images of the human thyroid microvessels. Red and blue represent flow directions. The white boxes denote the location of each slice 1, 2, and 3. UFD, ultrafast Doppler; US, ultrasound; 3D, three-dimensional. (a) and (b) © [2015] IEEE. Reprinted, with permission, from [95]. (c) and (d) Reproduced from [96]. CC BY 4.0.

spatiotemporal correlation [94]. This technique analyzes coherence across both spatial and temporal dimensions using an overlapping kernel, thereby providing a high-resolution evaluation of the imaging plane (figure 5(d)). To visualize microvascular blood flow in the human thyroid, 15 patients with suspected thyroid nodules were recruited. Their findings showed a significant improvement in microvascular visibility within the thyroid when the proposed method was applied (figure 5(e)).

Conventional linear-array transducers are widely used for Doppler and B-mode cross-sectional imaging. Although this approach effectively visualizes blood vessels in a cross-sectional view, it is limited in analyzing volumetric blood-flow dynamics. 3D images can be obtained through the elevational scanning of linear-array transducers; however, the resulting images often suffer from low spatial resolution due to the inherently poor elevational resolution of these transducers. To address these limitations, UFD imaging with 2D matrix array transducers was investigated. Provost *et al* introduced a 3D UFD imaging system capable of producing 572 US volumes per second [95]. This approach enables voxel-wise processing of Doppler signals, where each voxel within the 3D volume is individually processed (figure 6(a)). The feasibility of the 3D UFD system was demonstrated by imaging the thyroid region of a healthy volunteer (figure 6(b)). The high frame rate of volumetric image acquisition allows for real-time visualization of vascular structure and flow dynamics. However, despite these advancements, the resolution of 3D images remains lower than that of conventional cross-sectional images.

In a recent study, Hansen–Shearer *et al* enhanced the resolution of 3D UFD images through advanced processing techniques involving a contrast agent [96]. They employed a 2D row-column array transducer, which features fewer independent electronic channels and provides a wider FOV. This transducer comprises two orthogonally aligned series of elements, with a piezoelectric matrix positioned between the row and

column electrodes (figure 6(c)). This configuration significantly reduces the number of electrical channels, thereby lowering both the cost and complexity of the data acquisition module. The researchers improved image quality by integrating row-column array-specific coherence-based beamforming with acoustic sub-aperture processing techniques. The feasibility of this approach was evaluated through thyroid imaging in a healthy volunteer (figure 6(d)). By utilizing microbubbles as contrast agents, they significantly enhanced the localization and tracking of microvascular structures, resulting in detailed and high-resolution visualization of blood flow dynamics in the human thyroid.

5. Discussion and outlooks

Effective triaging of thyroid nodules requires high specificity to reduce the overdiagnosis of benign nodules while maintaining the sensitivity required for accurate detection of malignancy in conventional US-based risk stratification methods. Enhancing specificity can be achieved by incorporating functional information, as conventional techniques primarily provide structural data. Although US elastography has shown promise in improving classification accuracy [97–99], reproducibility and stability remain critical challenges for its successful clinical application. This review highlights recent advances in PAI and UFD techniques, particularly in analyzing vasculature-related characteristics of thyroid nodules.

PAI, which uses endogenous chromophores, including HbO, HbR, and lipids, has demonstrated promise in distinguishing malignant from benign thyroid nodules by calculating the sO_2 levels. The ability to extract functional information through multispectral PAI, combined with the familiarity of multimodal PAI and USI, positions it as a compelling candidate for clinical use. PAI has already been successfully applied in the assessment of other cancer types [100]. Notably, multispectral PAI in breast cancer analysis shows significant potential for classifying nodule malignancy. For instance, Neuschler *et al* reported that integrating multispectral PAI with the Breast Imaging Reporting and Data System (BI-RADS) improved diagnostic accuracy [101]. This finding was supported by a substantial sample size (1,079 benign and 678 malignant nodules) and comprehensive statistical analysis. Subsequent studies also confirmed that the PA-based BI-RADS correctly over diagnosed benign nodules, underscoring the feasibility of multispectral PAI in reducing over diagnosis [102]. Given these positive results, the method could be adapted for thyroid nodule assessment, potentially decreasing the need for unnecessary biopsies or surgical interventions by enhancing specificity.

Despite advancements in PAI, several challenges impede its clinical adoption. Although PAI offers relatively deep tissue penetration compared to other optical imaging techniques, light scattering within tissues degrades the SNR. Unlike the breast, which consists of relatively homogeneous tissue, the thyroid gland is encased in layers of muscle and skin. Strategies to enhance PAI performance, including optimization of transducer geometries, integration of appropriate US probes and optical fibers, and compensation techniques for light diffusion, warrant further investigation [103, 104]. Another limitation arises from the constrained FOV associated with linear array transducers typically employed in thyroid imaging. Innovations in wide-field 3D imaging techniques [105], deep learning methodologies [106–111], and novel image reconstruction methods [41, 112–115] could help address these challenges. Additionally, standardizing PAI systems is essential, as various components, such as lasers, transducers, image reconstruction algorithms, and display methods, are required for effective PAI implementation.

In contrast, UFD imaging significantly enhances visualization of the microvasculature in the thyroid gland. Recent advancements have effectively mitigated the challenges associated with motion artifacts caused by carotid pulsation through motion-corrected spatiotemporal filtering, thereby improving the clarity and accuracy of microvascular visualization. Compared to other US-based vascular imaging techniques, UFD demonstrates clinical feasibility for thyroid cancer assessment due to its highly sensitive, label-free approach. While power Doppler imaging can visualize blood flow intensity, its sensitivity to microvasculature detection is limited, leading to low specificity since intranodular vascularity is commonly observed in both benign and malignant nodules [28]. Superb microvascular imaging enhances microvascular visualization by filtering out motion artifacts, providing greater sensitivity than power Doppler imaging. However, it still lacks the capability for quantitative flow assessment, as it primarily displays the presence of blood flow [116]. In contrast, super-resolution US imaging surpasses diffraction limits by using microbubbles, enabling capillary-level resolution and quantitative evaluation of microvascular parameters such as flow rate and vessel density [117]. However, the use of exogenous contrast agents and complex post-processing may limits its clinical accessibility.

The introduction of 2D array transducers has enabled real-time 3D UFD imaging with higher spatial resolution than traditional linear array transducers, which often suffer from poor elevational resolution. The application of UFD extends beyond the thyroid gland to other organs. For example, Chen *et al* successfully visualized microvascular structures in the human kidney and breast using a 3D UFD with mechanically

scanned linear array transducers [118], whereas Provost *et al* achieved 3D UFD imaging of the human heart using a 2D matrix array transducer [119].

While these studies highlight the potential of UFD imaging for assessing malignancy in thyroid nodules, they remain in the experimental phase. Large-scale clinical trials are necessary to validate the accuracy, safety, and efficacy of this technique in human subjects. Such trials should compare UFD imaging with conventional risk stratification methods to demonstrate the clearly established. Similar to PAI, the standardization of UFD protocols is essential for its successful integration into clinical practice. However, UFD may enjoy a clinical acceptance advantage, as it does not require additional equipment beyond conventional US machines.

The clinical translation of PAI and UFD for thyroid nodule assessment requires a multi-phase process, including technical optimization, clinical validation, regulatory approval, and integration into routine clinical workflows. To facilitate widespread clinical adoption, the performance of PAI and UFD should be optimized for reliability, reproducibility, and user-friendliness. This entails advancements in hardware configuration and software algorithms, as well as the establishment of standardized imaging protocols to ensure consistency across different systems and institutions. For regulatory approval and clinical acceptance, large-scaled multi-center studies are essential to validate the efficacy of PAI and UFD in clinical settings. These studies should include diverse patient populations across multiple institutions. Following successful clinical validation, regulatory approval from agencies such as the United States Food and Drug Administration, the European Medicines Agency, or other national health agencies will be necessary to enable clinical adoption and widespread implementation.

In conclusion, this review provides an overview of the principles and characteristics of PAI and UFD, summarizing recent technological advancements in thyroid nodule assessment. Both modalities show promise in enhancing the triaging process by providing additional functional information that extends beyond traditional USI. Furthermore, PAI and UFD have been successfully applied to other organs, providing valuable insights for future thyroid studies. Integrating structural and functional information into existing US-based risk stratification methods has the potential to significantly improve the accuracy of thyroid nodule evaluations, ultimately reducing overdiagnosis and improving patient outcomes.

Data availability statement

The data cannot be made publicly available upon publication because they are owned by a third party and the terms of use prevent public distribution. The data that support the findings of this study are available upon reasonable request from the authors.

Acknowledgment

This research was supported by the Korean government: the National Research Foundation of Korea (NRF) Grants (RS-2021-NR060086, RS-2023-00236798, RS-2024-00340633, NRF-1711197526) funded by the Ministry of Science and ICT.

ORCID iDs

Jean-Claude Vial https://orcid.org/0000-0003-2658-4270
Wonseok Choi https://orcid.org/0000-0002-7239-1237

References

[1] Huang J, Ngai C H, Deng Y, Pun C N, Lok V, Zhang L, Xu Q, Lucero-Prisno D E, Xu W and Zheng Z-J 2023 Incidence and mortality of thyroid cancer in 50 countries: a joinpoint regression analysis of global trends *Endocrine* **80** 355–65
[2] Megwalu U and Moon P K 2022 Thyroid cancer incidence and mortality trends in the United States: 2000–2018 *Thyroid* **32** 560–70
[3] Yu J 2024 Trends in the incidence of thyroid cancer among US persons from 2000 to 2019 *Eur. J. Cancer Prevention* **33** 5–10
[4] Boucai L, Zafereo M and Cabanillas M E 2024 Thyroid cancer: a review *JAMA* **331** 425–35
[5] Kim D, Li G, Moon P K, Ma Y, Sim S, Park S Y, Oh M and Megwalu U C 2024 Thyroid cancer incidence Among Korean individuals: a comparison of South Korea and the United States *Laryngoscope* **134** 4156–60
[6] American Cancer Society - Cancer Statistics Center (available at: https://cancerstatisticscenter.cancer.org)
[7] Davies L, Morris L G, Haymart M, Chen A Y, Goldenberg D, Morris J, Ogilvie J B, Terris D J, Netterville J and Wong R J 2015 American association of clinical endocrinologists and American college of endocrinology disease state clinical review: the increasing incidence of thyroid cancer *Endocr. Pract.* **21** 686–96
[8] Sajisevi M, Caulley L, Eskander A, Du Y J, Auh E, Karabachev A, Callas P, Conradie W, Martin L and Pasternak J 2022 Evaluating the rising incidence of thyroid cancer and thyroid nodule detection modes: a multinational, multi-institutional analysis *JAMA Otolaryngol. Head Neck Surg.* **148** 811–8

[9] Tao Z, Deng X, Guo B, Ding Z and Fan Y 2024 Subgroup analysis of steadily increased trends in medullary thyroid carcinoma incidence and mortality in the USA, 2000–2020: a population-based retrospective cohort study *Endocrine-Relat. Cancer* **31** e230319
[10] Ullmann T M, Papaleontiou M and Sosa J A 2023 Current controversies in low-risk differentiated thyroid cancer: reducing overtreatment in an era of overdiagnosis *J. Clin. End. Metab.* **108** 271–80
[11] Chen D W, Lang B H, McLeod D S, Newbold K and Haymart M R 2023 Thyroid cancer *Lancet* **401** 1531–44
[12] Haymart M R, Banerjee M, Reyes-Gastelum D, Caoili E and Norton E C 2019 Thyroid ultrasound and the increase in diagnosis of low-risk thyroid cancer *J. Clin. End. Metab.* **104** 785–92
[13] Hegedüs L 2004 The thyroid nodule *New Engl. J. Med.* **351** 1764–71
[14] Vaccarella S, Franceschi S, Bray F, Wild C P, Plummer M and Dal Maso L 2016 Worldwide thyroid-cancer epidemic? The increasing impact of overdiagnosis *New Engl. J. Med.* **375** 614–7
[15] Haugen B R, Alexander E K, Bible K C, Doherty G M, Mandel S J, Nikiforov Y E, Pacini F, Randolph G W, Sawka A M and Schlumberger M 2016 2015 American thyroid association management guidelines for adult patients with thyroid nodules and differentiated thyroid cancer: the american thyroid association guidelines task force on thyroid nodules and differentiated thyroid cancer *Thyroid* **26** 1–133
[16] Perros P, Boelaert K, Colley S, Evans C, Evans R M, Gerrard B A G, Gilbert J, Harrison B, Johnson S J and Giles T E 2014 Guidelines for the management of thyroid cancer *Clin. End.* **81** 1–122
[17] Kwak J Y, Han K H, Yoon J H, Moon H J, Son E J, Park S H, Jung H K, Choi J S, Kim B M and Kim E-K 2011 Thyroid imaging reporting and data system for US features of nodules: a step in establishing better stratification of cancer risk *Radiology* **260** 892–9
[18] Moon W-J, Jung S L, Lee J H, Na D G, Baek J-H, Lee Y H, Kim J, Kim H S, Byun J S and Lee D H 2008 Benign and malignant thyroid nodules: US differentiation—multicenter retrospective study *Radiology* **247** 762–70
[19] Frates M C, Benson C B, Charboneau J W, Cibas E S, Clark O H, Coleman B G, Cronan J J, Doubilet P M, Evans D B and Goellner J R 2005 Management of thyroid nodules detected at US: society of radiologists in ultrasound consensus conference statement *Radiology* **237** 794–800
[20] Cooper D S, Doherty G M, Haugen B R, Kloos R T, Lee S L, Mandel S J, Mazzaferri E L, McIver B, Sherman S I and Tuttle R M 2006 Management guidelines for patients with thyroid nodules and differentiated thyroid cancer: the American thyroid association guidelines taskforce *Thyroid* **16** 109–42
[21] Ahn H S, Kim H J and Welch H G 2014 Korea's thyroid-cancer "Epidemic"—screening and overdiagnosis *New Engl. J. Med.* **371** 1765–7
[22] Welch H G and Black W C 2010 Overdiagnosis in cancer *J. Nat. Cancer Inst.* **102** 605–13
[23] Dedhia P H, Saucke M C, Long K L, Doherty G M and Pitt S C 2022 Physician perspectives of overdiagnosis and overtreatment of low-risk papillary thyroid cancer in the US *JAMA Netw. Open* **5** e228722
[24] Park B, Kim C and Kim J 2023 Recent advances in ultrasound and photoacoustic analysis for thyroid cancer diagnosis *Adv. Phys. Res.* **2** 2200070
[25] Appetecchia M and Solivetti F 2006 The association of colour flow doppler sonography and conventional ultrasonography improves the diagnosis of thyroid carcinoma *Horm. Res. Paediatr.* **66** 249–56
[26] Rosario P W, Silva A L D, Borges M A R and Calsolari M R 2015 Is doppler ultrasound of additional value to gray-scale ultrasound in differentiating malignant and benign thyroid nodules? *Arch. End. Metab.* **59** 79–83
[27] Zhu Y C, Du H, Jiang Q, Zhang T, Huang X J, Zhang Y, Shi X R, Shan J and AlZoubi A 2021 Machine learning assisted doppler features for enhancing thyroid cancer diagnosis: a multi-cohort study *J. Ultrasound Med.* **41** 1961–74
[28] Moon H J, Kwak J Y, Kim M J, Son E J and Kim E-K 2010 Can vascularity at power doppler US help predict thyroid malignancy? *Radiology* **255** 260–9
[29] Yoon J H, Kim E-K, Kwak J Y, Park V Y and Moon H J 2018 Application of various additional imaging techniques for thyroid ultrasound: direct comparison of combined various elastography and doppler parameters to gray-scale ultrasound in differential diagnosis of thyroid nodules *Ultrasound Med. Biol.* **44** 1679–86
[30] Khadra H, Bakeer M, Hauch A, Hu T and Kandil E 2016 Is vascular flow a predictor of malignant thyroid nodules? A meta-analysis *Gland Surg.* **5** 576
[31] Maddaloni E, Briganti S I, Crescenzi A, Anguissola G B, Perrella E, Taffon C, Palermo A, Manfrini S, Pozzilli P and Pantano A L 2021 Usefulness of color doppler ultrasonography in the risk stratification of thyroid nodules *Eur. Thyroid J.* **10** 339–44
[32] Nabhan F and Ringel M D 2017 Thyroid nodules and cancer management guidelines: comparisons and controversies *Endocrine-Relat. Cancer* **24** R13–R26
[33] Xia J, Yao J and Wang L V 2014 Photoacoustic tomography: principles and advances *Prog. Electromagn. Res.* **147** 1–22
[34] Han S, Lee H, Kim C and Kim J 2022 Review on multispectral photoacoustic analysis of cancer: thyroid and breast *Metabolites* **12** 382
[35] Attia A B E, Balasundaram G, Moothanchery M, Dinish U, Bi R, Ntziachristos V and Olivo M 2019 A review of clinical photoacoustic imaging: current and future trends *Photoacoustics* **16** 100144
[36] Lee H, Choi W, Kim C, Park B and Kim J 2023 Review on ultrasound-guided photoacoustic imaging for complementary analyses of biological systems *in vivo Exp. Biol. Med.* **248** 762–74
[37] Lee H, Han S, Kye H, Kim T-K, Choi W and Kim J 2023 A review on the roles of photoacoustic imaging for conventional and novel clinical diagnostic applications *Photonics* **10** 904
[38] Park E-Y, Lee H, Han S, Kim C and Kim J 2022 Photoacoustic imaging systems based on clinical ultrasound platform *Exp. Biol. Med.* **247** 551–60
[39] Steinberg I, Huland D M, Vermesh O, Frostig H E, Tummers W S and Gambhir S S 2019 Photoacoustic clinical imaging *Photoacoustics* **14** 77–98
[40] Osmanski B-F, Pernot M, Montaldo G, Bel A, Messas E and Tanter M 2012 Ultrafast Doppler imaging of blood flow dynamics in the myocardium *IEEE Trans. Med. Imaging* **31** 1661–8
[41] Xu M and Wang L V 2005 Universal back-projection algorithm for photoacoustic computed tomography *Phys. Rev.* E **71** 016706
[42] Zhou Y, Yao J and Wang L V 2016 Tutorial on photoacoustic tomography *J. Biomed. Opt.* **21** 061007
[43] Choi W, Oh D and Kim C 2020 Practical photoacoustic tomography: realistic limitations and technical solutions *J. Appl. Phys.* **127** 230903
[44] Deán-Ben X L and Razansky D 2016 On the link between the speckle free nature of optoacoustics and visibility of structures in limited-view tomography *Photoacoustics* **4** 133–40
[45] Bushberg J T and Boone J M 2011 *The Essential Physics of Medical Imaging* (Lippincott Williams & Wilkins)

[46] Demené C, Deffieux T, Pernot M, Osmanski B-F, Biran V, Gennisson J-L, Sieu L-A, Bergel A, Franqui S and Correas J-M 2015 Spatiotemporal clutter filtering of ultrafast ultrasound data highly increases Doppler and fUltrasound sensitivity *IEEE Trans. Med. Imaging* **34** 2271–85
[47] Huang C, Song P, Gong P, Trzasko J D, Manduca A and Chen S 2019 Debiasing-based noise suppression for ultrafast ultrasound microvessel imaging *IEEE Trans. Ultrason. Ferroelectr. Freq. Control* **66** 1281–91
[48] Wang L V and Hu S 2012 Photoacoustic tomography: *in vivo* imaging from organelles to organs *Science* **335** 1458–62
[49] Kim C, Favazza C and Wang L V 2010 *In vivo* photoacoustic tomography of chemicals: high-resolution functional and molecular optical imaging at new depths *Chem. Rev.* **110** 2756–82
[50] Choi W, Park B, Choi S, Oh D, Kim J and Kim C 2023 Recent advances in contrast-enhanced photoacoustic imaging: overcoming the physical and practical challenges *Chem. Rev.* **123** 7379–419
[51] Park B, Oh D, Kim J and Kim C 2023 Functional photoacoustic imaging: from nano-and micro-to macro-scale *Nano Converg.* **10** 29
[52] Han S, Lee D, Kim S, Kim H-H, Jeong S and Kim J 2022 Contrast agents for photoacoustic imaging: a review focusing on the wavelength range *Biosensors* **12** 594
[53] Zhang Y, Jeon M, Rich L J, Hong H, Geng J, Zhang Y, Shi S, Barnhart T E, Alexandridis P and Huizinga J D 2014 Non-invasive multimodal functional imaging of the intestine with frozen micellar naphthalocyanines *Nat. Nanotechnol.* **9** 631–8
[54] Jung H *et al* 2019 A peptide probe enables pphotoacoustic-guided imaging and drug delivery to lung tumors in K-rasLA2 mutant mice *Cancer Res.* **79** 4271–82
[55] Choi W *et al* 2022 Three-dimensional multistructural quantitative photoacoustic and US imaging of human feet *in vivo Radiology* **303** 467–73
[56] Ivankovic I, Merčep E, Schmedt C-G, Deán-Ben X L and Razansky D 2019 Real-time volumetric assessment of the human carotid artery: handheld multispectral optoacoustic tomography *Radiology* **291** 45–50
[57] Kim J, Kim Y H, Park B, Seo H M, Bang C H, Park G S, Park Y M, Rhie J W, Lee J H and Kim C 2018 Multispectral *ex vivo* photoacoustic imaging of cutaneous melanoma for better selection of the excision margin *Br. J. Dermatol.* **179** 780–2
[58] Lin L, Hu P, Shi J, Appleton C M, Maslov K, Li L, Zhang R and Wang L V 2018 Single-breath-hold photoacoustic computed tomography of the breast *Nat. Commun.* **9** 2352
[59] Knieling F, Neufert C, Hartmann A, Claussen J, Urich A, Egger C, Vetter M, Fischer S, Pfeifer L and Hagel A 2017 Multispectral optoacoustic tomography for assessment of Crohn's disease activity *New Engl. J. Med.* **376** 1292–4
[60] Kukačka J, Metz S, Dehner C, Muckenhuber A, Paul-Yuan K, Karlas A, Fallenberg E M, Rummeny E, Jüstel D and Ntziachristos V 2022 Image processing improvements afford second-generation handheld optoacoustic imaging of breast cancer patients *Photoacoustics* **26** 100343
[61] Nyayapathi N and Xia J 2019 Photoacoustic imaging of breast cancer: a mini review of system design and image features *J. Biomed. Opt.* **24** 121911
[62] Diot G, Metz S, Noske A, Liapis E, Schroeder B, Ovsepian S V, Meier R, Rummeny E and Ntziachristos V 2017 Multispectral optoacoustic tomography (MSOT) of human breast cancer *Clin. Cancer Res.* **23** 6912–22
[63] Park B, Bang C H, Lee C, Han J H, Choi W, Kim J, Park G S, Rhie J W, Lee J H and Kim C 2020 3D wide-field multispectral photoacoustic imaging of human melanomas *in vivo*: a pilot study *J. Eur. Acad. Dermatol. Venereol.* **35** 669–76
[64] Zhou Y, Tripathi S V, Rosman I, Ma J, Hai P, Linette G P, Council M L, Fields R C, Wang L V and Cornelius L A 2017 Noninvasive determination of melanoma depth using a handheld photoacoustic probe *J. Invest. Dermatol.* **137** 1370–2
[65] Zhou Y, Li G, Zhu L, Li C, Cornelius L A and Wang L V 2015 Handheld photoacoustic probe to detect both melanoma depth and volume at high speed *in vivo J. Biophoton.* **8** 961–7
[66] Kothapalli S-R *et al* 2019 Simultaneous transrectal ultrasound and photoacoustic human prostate imaging *Sci. Trans. Med.* **11** eaav2169
[67] Horiguchi A, Shinchi M, Nakamura A, Wada T, Ito K, Asano T, Shinmoto H, Tsuda H and Ishihara M 2017 Pilot study of prostate cancer angiogenesis imaging using a photoacoustic imaging system *Urology* **108** 212–9
[68] Horiguchi A, Tsujita K, Irisawa K, Kasamatsu T, Hirota K, Kawaguchi M, Shinchi M, Ito K, Asano T and Shinmoto H 2016 A pilot study of photoacoustic imaging system for improved real-time visualization of neurovascular bundle during radical prostatectomy *Prostate* **76** 307–15
[69] Kang J, Chung W Y, Kang S-W, Kwon H J, Yoo J, Kim E-K, Chang J H, Song T-K, Lee S and Kwak J Y 2014 *Ex vivo* estimation of photoacoustic imaging for detecting thyroid microcalcifications *PLoS One* **9** e113358
[70] Dogra V S, Chinni B K, Valluru K S, Moalem J, Giampoli E J, Evans K and Rao N A 2014 Preliminary results of *ex vivo* multispectral photoacoustic imaging in the management of thyroid cancer *Am. J. Roentgenol.* **202** W552–W8
[71] Sinha S, Dogra V S, Chinni B K and Rao N A 2017 Frequency domain analysis of multiwavelength photoacoustic signals for differentiating among malignant, benign, and normal thyroids in an ex vivo study with human thyroids *J. Ultrasound Med.* **36** 2047–59
[72] Dima A and Ntziachristos V 2016 *In-vivo* handheld optoacoustic tomography of the human thyroid *Photoacoustics* **4** 65–69
[73] Yang M, Zhao L, He X, Su N, Zhao C, Tang H, Hong T, Li W, Yang F and Lin L 2017 Photoacoustic/ultrasound dual imaging of human thyroid cancers: an initial clinical study *Biomed. Opt. Express* **8** 3449–57
[74] Roll W, Markwardt N A, Masthoff M, Helfen A, Claussen J, Eisenblätter M, Hasenbach A, Hermann S, Karlas A and Wildgruber M 2019 Multispectral optoacoustic tomography of benign and malignant thyroid disorders: a pilot study *J. Nucl. Med.* **60** 1461–6
[75] Noltes M E, Bader M, Metman M J, Vonk J, Steinkamp P J, Kukačka J, Westerlaan H E, Dierckx R A, van Hemel B M and Brouwers A H 2023 Towards *in vivo* characterization of thyroid nodules suspicious for malignancy using multispectral optoacoustic tomography *Eur. J. Nucl. Med. Mol. Imaging* **50** 2736–50
[76] Kim J *et al* 2021 Multiparametric photoacoustic analysis of human thyroid cancers *in vivo Cancer Res.* **81** 4849–60
[77] Becker A, Masthoff M, Claussen J, Ford S J, Roll W, Burg M, Barth P J, Heindel W, Schaefers M and Eisenblaetter M 2018 Multispectral optoacoustic tomography of the human breast: characterisation of healthy tissue and malignant lesions using a hybrid ultrasound-optoacoustic approach *Eur. Radiol.* **28** 602–9
[78] Kim J, Park S, Jung Y, Chang S, Park J, Zhang Y, Lovell J F and Kim C 2016 Programmable real-time clinical photoacoustic and ultrasound imaging system *Sci. Rep.* **6** 35137
[79] Chen F, Han H, Wan P, Chen L, Kong W, Liao H, Wen B, Liu C and Zhang D 2024 Do as sonographers think: contrast-enhanced ultrasound for thyroid nodules diagnosis via microvascular infiltrative awareness *IEEE Trans. Med. Imaging* **43** 3881–94
[80] Liu M and Pan N 2024 Quantitative ultrasound imaging parameters in patients with cancerous thyroid nodules: development of a diagnostic model *Am. J. Transl. Res.* **16** 2645

[81] Akhoundi N, Naseri Z, Siami A, Hazara S, Noorbakhsh M, Hazara K and Rezazadeh E 2024 Exploring the diagnostic role of spectral doppler as a predictor of malignancy within thyroid nodules *J. Diagn. Med. Sonogr.* **40** 29–36
[82] Li W, Gao L, Du Y, Wang Y, Yang X, Wang H and Li J 2024 Ultrasound microflow patterns help in distinguishing malignant from benign thyroid nodules *Cancer Imaging* **24** 18
[83] Huang T, Huang P-T, Luo Z-Y, Lv J-F, Jin P-L, Zhang T, Zhao Y-L, Wang Y and Hong Y-R 2024 Use superb microvascular imaging to diagnose and predict metastatic cervical lymph nodes in patients with papillary thyroid carcinoma *J. Cancer Res. Clin. Oncol.* **150** 268
[84] Suh P S, Baek J H, Lee J H, Chung S R, Choi Y J, Chung K-W, Kim T Y and Lee J H 2024 Effectiveness of microvascular flow imaging for radiofrequency ablation in recurrent thyroid cancer: comparison with power Doppler imaging *Eur. Radiol.* **35** 1–11
[85] Chen Y, Fang B, Meng F, Luo J and Luo X 2024 Competitive swarm optimized SVD clutter filtering for ultrafast power Doppler imaging *IEEE Trans. Ultrason. Ferroelectr. Freq. Control* **71** 459–73
[86] Demené C, Tiran E, Sieu L-A, Bergel A, Gennisson J L, Pernot M, Deffieux T, Cohen I and Tanter M 2016 4D microvascular imaging based on ultrafast Doppler tomography *Neuroimage* **127** 472–83
[87] Oh D, Lee D, Heo J, Kweon J, Yong U, Jang J, Ahn Y J and Kim C 2023 Contrast agent-free 3D renal ultrafast Doppler imaging reveals vascular dysfunction in acute and diabetic kidney diseases *Adv. Sci.* **10** 2303966
[88] Villemain O, Baranger J, Friedberg M K, Papadacci C, Dizeux A, Messas E, Tanter M, Pernot M and Mertens L 2020 Ultrafast ultrasound imaging in pediatric and adult cardiology: techniques, applications, and perspectives *Cardiovascular Imaging* **13** 1771–91
[89] Matrone G, Savoia A S, Caliano G and Magenes G 2016 Ultrasound plane-wave imaging with delay multiply and sum beamforming and coherent compounding *Proc. 2016 38th Annual Int. Conf. of the IEEE Engineering in Medicine and Biology Society (EMBC)*
[90] Bercoff J, Montaldo G, Loupas T, Savery D, Mézière F, Fink M and Tanter M 2011 Ultrafast compound Doppler imaging: providing full blood flow characterization *IEEE Trans. Ultrason. Ferroelectr. Freq. Control* **58** 134–47
[91] Baranger J, Arnal B, Perren F, Baud O, Tanter M and Demené C 2018 Adaptive spatiotemporal SVD clutter filtering for ultrafast Doppler imaging using similarity of spatial singular vectors *IEEE Trans. Med. Imaging* **37** 1574–86
[92] Nayak R, Kumar V, Webb J, Fatemi M and Alizad A 2019 Non-invasive small vessel imaging of human thyroid using motion-corrected spatiotemporal clutter filtering *Ultrasound Med. Biol.* **45** 1010–8
[93] Nayak R, Nawar N, Webb J, Fatemi M and Alizad A 2020 Impact of imaging cross-section on visualization of thyroid microvessels using ultrasound: pilot study *Sci. Rep.* **10** 415
[94] Nayak R, MacNeill J, Flores C, Webb J, Fatemi M and Alizad A 2021 Quantitative assessment of ensemble coherency in contrast-free ultrasound microvasculature imaging *Med. Phys.* **48** 3540–58
[95] Provost J, Papadacci C, Demene C, Gennisson J-L, Tanter M and Pernot M 2015 3-D ultrafast Doppler imaging applied to the noninvasive mapping of blood vessels *in vivo IEEE Trans. Ultrason. Ferroelectr. Freq. Control* **62** 1467–72
[96] Hansen-Shearer J, Yan J, Lerendegui M, Huang B, Toulemonde M, Riemer K, Tan Q, Tonko J, Weinberg P D and Dunsby C 2024 Ultrafast 3-D transcutaneous super resolution ultrasound using row-column array specific coherence-based beamforming and rolling acoustic sub-aperture processing: *in vitro*, in rabbit and in human study *Ultrasound Med. Biol.* **50** 1045–57
[97] Zhao C-K and Xu H-X 2019 Ultrasound elastography of the thyroid: principles and current status *Ultrasonography* **38** 106
[98] Prado-Costa R, Rebelo J, Monteiro-Barroso J and Preto A S 2018 Ultrasound elastography: compression elastography and shear-wave elastography in the assessment of tendon injury *Insights into Imaging* **9** 791–814
[99] Ozturk A, Grajo J R, Dhyani M, Anthony B W and Samir A E 2018 Principles of ultrasound elastography *Abdom. Radiol.* **43** 773–85
[100] Park J, Choi S, Knieling F, Clingman B, Bohndiek S, Wang L V and Kim C 2024 Clinical translation of photoacoustic imaging *Nat. Rev. Bioeng.* **3** 1–20
[101] Neuschler E I, Butler R, Young C A, Barke L D, Bertrand M L, Böhm-Vélez M, Destounis S, Donlan P, Grobmyer S R and Katzen J 2017 A pivotal study of optoacoustic imaging to diagnose benign and malignant breast masses: a new evaluation tool for radiologists *Radiology* **287** 398–412
[102] Menezes G L, Pijnappel R M, Meeuwis C, Bisschops R, Veltman J, Lavin P T, Van De Vijver M J and Mann R M 2018 Downgrading of breast masses suspicious for cancer by using optoacoustic breast imaging *Radiology* **288** 355–65
[103] Kim J, Park E-Y, Park B, Choi W, Lee K J and Kim C 2020 Towards clinical photoacoustic and ultrasound imaging: probe improvement and real-time graphical user interface *Exp. Biol. Med.* **245** 321–9
[104] Zhao L, Yang M, Jiang Y and Li C 2017 Optical fluence compensation for handheld photoacoustic probe: an *in vivo* human study case *J. Innov. Opt. Health Sci.* **10** 174002
[105] Lee C, Cho S, Lee D, Lee J, Park J-I, Kim H-J, Park S H, Choi W, Kim U and Kim C 2023 Panoramic volumetric clinical handheld photoacoustic and ultrasound imaging *Photoacoustics* **31** 100512
[106] Kim J, Kim G, Li L, Zhang P, Kim J Y, Kim Y, Kim H H, Wang L V, Lee S and Kim C 2022 Deep learning acceleration of multiscale superresolution localization photoacoustic imaging *Light Sci. Appl.* **11** 1–12
[107] Ly C D, Vo T H, Mondal S, Park S, Choi J, Vu T T H, Kim C-S and Oh J 2022 Full-view *in vivo* skin and blood vessels profile segmentation in photoacoustic imaging based on deep learning *Photoacoustics* **25** 100310
[108] Jeon S, Choi W, Park B and Kim C 2021 A deep learning-based model that reduces speed of sound aberrations for improved *in vivo* photoacoustic imaging *IEEE Trans. Image Process.* **30** 8773–84
[109] Yang C, Lan H, Gao F and Gao F 2021 Review of deep learning for photoacoustic imaging *Photoacoustics* **21** 100215
[110] Guan S, Khan A A, Sikdar S and Chitnis P V 2020 Limited-view and sparse photoacoustic tomography for neuroimaging with deep learning *Sci. Rep.* **10** 1–12
[111] Kim J, Lee D, Lim H, Yang H, Kim J, Kim J, Kim Y, Kim H H and Kim C 2022 Deep learning alignment of bidirectional raster scanning in high speed photoacoustic microscopy *Sci. Rep.* **12** 1–10
[112] Park J, Jeon S, Meng J, Song L, Lee J S and Kim C 2016 Delay-multiply-and-sum-based synthetic aperture focusing in photoacoustic microscopy *J. Biomed. Opt.* **21** 036010
[113] Rosenthal A, Razansky D and Ntziachristos V 2010 Fast semi-analytical model-based acoustic inversion for quantitative optoacoustic tomography *IEEE Trans. Med. Imaging* **29** 1275–85
[114] Nasiriavanaki M, Xia J, Wan H, Bauer A Q, Culver J P and Wang L V 2014 High-resolution photoacoustic tomography of resting-state functional connectivity in the mouse brain *Proc. Natl Acad. Sci. USA* **111** 21–26
[115] Zhang C and Wang Y 2008 A reconstruction algorithm for thermoacoustic tomography with compensation for acoustic speed heterogeneity *Phys. Med. Biol.* **53** 4971

[116] Li W, Ge Z, Cai S, Fang S, Zhang M, Wang H and Li J 2024 Diagnostic value of greyscale ultrasound combined with superb microvascular imaging in thyroid nodules: a systematic review and meta-analysis *Quant. Imaging Med. Surg.* **15** 440
[117] Zhang G, Yu J, Lei Y-M, Hu J-R, Hu H-M, Harput S, Guo Z-Z, Cui X-W and Ye H-R 2022 Ultrasound super-resolution imaging for the differential diagnosis of thyroid nodules: a pilot study *Front. Oncol.* **12** 978164
[118] Chen C, Hendriks G A, Fekkes S, Mann R M, Menssen J, Siebers C C, de Korte C L and Hansen H H 2022 *In vivo* 3D power Doppler imaging using continuous translation and ultrafast ultrasound *IEEE Trans. Biomed. Eng.* **69** 1042–51
[119] Provost J, Papadacci C, Arango J E, Imbault M, Fink M, Gennisson J-L, Tanter M and Pernot M 2014 3D ultrafast ultrasound imaging *in vivo Phys. Med. Biol.* **59** L1